

# n-Fe<sub>2</sub>O<sub>3</sub> to N<sup>+</sup>-TiO<sub>2</sub> Heterojunction Photoanode for Photoelectrochemical Water Oxidation

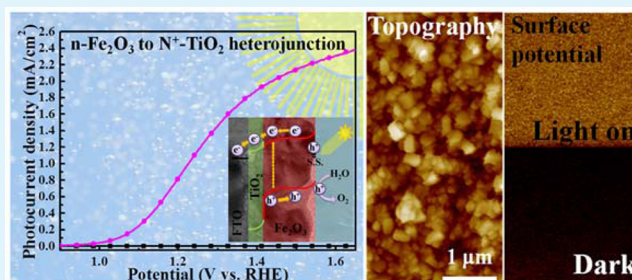
Jih-Sheng Yang,<sup>†</sup> Wan-Hsien Lin,<sup>‡</sup> Chia-Yu Lin,<sup>†</sup> Bo-Sheng Wang,<sup>†</sup> and Jih-Jen Wu<sup>\*†</sup>

<sup>†</sup>Department of Chemical Engineering and <sup>‡</sup>Promotion Center for Global Materials Research (PCGMR), Department of Materials Science and Engineering, National Cheng Kung University, Tainan 70101, Taiwan

## Supporting Information

**ABSTRACT:** To improve the performance of the thin hematite photoanode for photoelectrochemical water oxidation, in this work, an nN<sup>+</sup>  $\alpha$ -Fe<sub>2</sub>O<sub>3</sub> (hematite)-TiO<sub>2</sub> heterojunction photoanode is constructed on fluorine-doped tin oxide substrate to establish a built-in field in the space charge region for facilitating the charge separation in the hematite layer. Charge distribution in the hematite-TiO<sub>2</sub> heterostructure is investigated using Kelvin probe force microscopy, which confirms the improvement of charge separation in hematite layer by the formation of energy-matched nN<sup>+</sup>  $\alpha$ -Fe<sub>2</sub>O<sub>3</sub>-TiO<sub>2</sub> heterojunction. Compared to the hematite photoanode, an eightfold enhancement of the photocurrent density at 1.23 V versus reversible hydrogen electrode is measured in the hematite-TiO<sub>2</sub> heterojunction photoanode. By using hydrogen peroxide as a hole scavenger, it demonstrates that both charge separation and charge injection efficiencies in the hematite-TiO<sub>2</sub> heterojunction photoanode are superior to those in the hematite photoanode. It results from the significant suppressions of the charge recombinations occurring within the hematite layer as well as at the interface of photoelectrode and electrolyte by the formation of the nN<sup>+</sup>  $\alpha$ -Fe<sub>2</sub>O<sub>3</sub>-TiO<sub>2</sub> heterojunction.

**KEYWORDS:** photoelectrochemical water oxidation, hematite, titanium dioxide, heterojunction, charge separation



## INTRODUCTION

In addition to the direct conversion of solar energy to electrical power by photovoltaic solar cells, the production of solar fuels that store solar energy in the form of chemical bonds is a promising technique for the practical utilization of the most abundant renewable energy source.<sup>1</sup> Efficient conversion of solar energy to the simplest solar fuel of H<sub>2</sub> can be realized using semiconductor electrodes in a photoelectrochemical (PEC) water-splitting cell.<sup>2,3</sup> Hematite ( $\alpha$ -Fe<sub>2</sub>O<sub>3</sub>), which is an n-type semiconductor, possesses an appropriate band gap of 2.0–2.2 eV for solar light harvesting and a suitable energy level of valence band edge for water oxidation. With additional advantages of abundance, nontoxicity, and good chemical stability in aqueous environments, hematite has therefore been proposed to be one of the most promising photoanode materials for use in PEC water-splitting cells.<sup>4,5</sup>

However, several drawbacks of hematite, such as short charge diffusion length, slow hole kinetics of the oxygen evolution reaction, significant charge trapping in surface states, and slightly positive conduction band edge to the H<sup>+</sup>/H<sub>2</sub> redox potential, limit its PEC efficiency.<sup>4,5</sup> To enhance the performance of the hematite photoanodes, the strategies of the miniaturization of the dimensions of hematite nanostructures and the surface modification of the thin hematite layer with water oxidation catalysts have been demonstrated to increase the photocurrent and to decrease the overpotential, respectively.<sup>4–7</sup> Formation of n–p hematite homojunction has also

been reported to efficiently decrease the onset potential in the absence of water oxidation catalyst.<sup>8</sup> Moreover, the PEC performance of the thin hematite photoanode has been improved by the addition of an underlayer, which results from the enhancement of the crystallinity of thin hematite layer<sup>9,10</sup> or the suppression of the electron back injection from conducting substrate to hematite.<sup>11</sup>

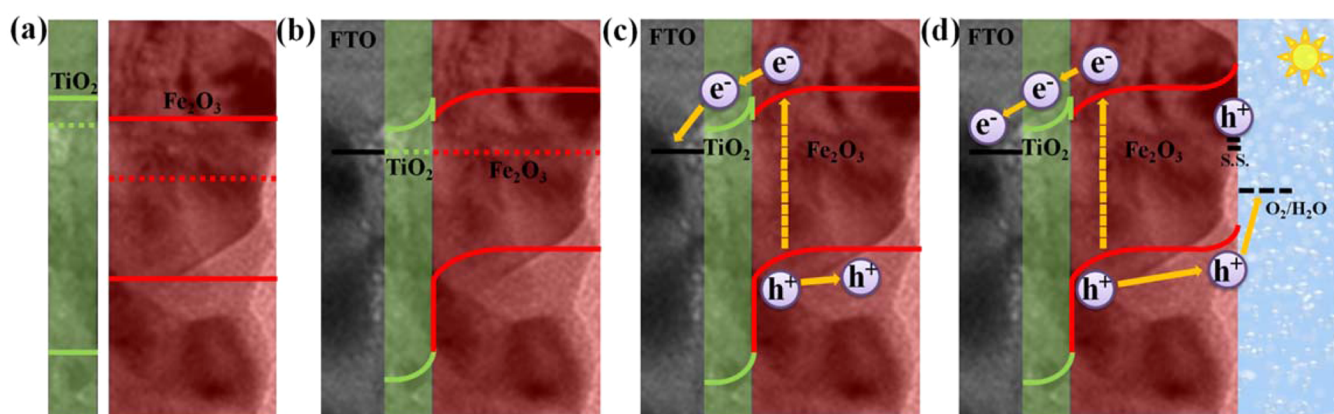
Hematite exhibits short hole diffusion length and high-density surface states that bring about the severe recombination of the photogenerated charges occurring in the bulk and surface states. The photogenerated holes in the hematite are therefore unable to efficiently reach the surface and inject into electrolyte for water oxidation, which have been proposed to be the key loss pathways in hematite.<sup>4,5</sup> Efficient charge separation for the reduction of recombination of photogenerated charges plays a crucial role in the enhancement of the PEC performance of the hematite photoanode.<sup>4–7</sup> In this work, a low-cost hematite-TiO<sub>2</sub> heterojunction is designed for establishing a built-in field in the space charge region to facilitate the charge separation in the hematite layer and therefore to improve the PEC performance of the hematite photoanode. However, a challenge to the configuration is that the conduction band edge (E<sub>c</sub>) of the hematite is slightly positive to that of TiO<sub>2</sub>,<sup>12</sup> as illustrated

Received: February 14, 2015

Accepted: June 1, 2015

Published: June 1, 2015

Scheme 1. Schematic Diagrams Illustrating the Respective Band Positions and Photogenerated Charge Separation in the  $n\text{N}^+ \alpha\text{-Fe}_2\text{O}_3\text{-TiO}_2$  Heterojunction Photoanodes for Photoelectrochemical Water Oxidation<sup>a</sup>



<sup>a</sup>(a) Band diagrams for  $n\text{N}^+ \alpha\text{-Fe}_2\text{O}_3\text{-TiO}_2$  before joining. (b) Equilibrium band diagram for the junction in dark. (c) Band diagram for the junction under illumination. (d) Band diagram for the junction in electrolyte under illumination.

in Scheme 1a. In this aspect, a heavily doped ( $\text{N}^+$ )  $\text{TiO}_2$  and a lightly doped ( $\text{n}^-$ ) hematite are essential for the heterojunction formation to ensure the energy match between the conduction band edges of hematite and  $\text{TiO}_2$  as well as to enlarge the width of the space charge region in the hematite film (Scheme 1b). Under irradiation, the photoelectrons are therefore able to efficiently transfer from hematite through  $\text{TiO}_2$  to electrode, as shown in Scheme 1c.

To construct such  $n\text{N}^+ \alpha\text{-Fe}_2\text{O}_3\text{-TiO}_2$  heterojunctions on the fluorine-doped tin oxide (FTO) substrates, the  $\text{TiO}_2$  nanostructures are formed on FTO substrates using wet chemical routes,<sup>3,13</sup> and high-quality hematite films are sequentially grown on the  $\text{TiO}_2$  layers by chemical vapor deposition (CVD).<sup>14</sup> Charge distribution in the hematite- $\text{TiO}_2$  heterostructure is investigated using Kelvin probe force microscopy (KPFM),<sup>15,16</sup> which determines the improvement of charge separation in hematite layer by the formation of energy-matched  $n\text{N}^+ \alpha\text{-Fe}_2\text{O}_3\text{-TiO}_2$  heterojunction on FTO substrate. Compared to the hematite photoanode, significant enhancement in PEC performance is demonstrated in the hematite- $\text{TiO}_2$  heterojunction photoanodes. By using hydrogen peroxide as a hole scavenger,<sup>17</sup> it reveals that both charge separation and injection efficiencies in the  $n\text{N}^+ \alpha\text{-Fe}_2\text{O}_3\text{-TiO}_2$  heterojunction photoanode are increased compared to those in hematite photoanode.

## EXPERIMENTAL SECTION

Two types of rutile  $\text{TiO}_2$  nanostructures were deposited on FTO substrate. The  $\text{TiO}_2$  disjointed nanostructure (DNS) was grown on FTO substrate by hydrothermal method<sup>3,13</sup> using a solution of 40 mL of 8 M HCl in deionized water and 0.5 mL of titanium(IV) *tert*-n-butoxide at 150 °C for 3.5 h. To further develop  $\text{TiO}_2$  continuous nanostructure (CNS) from the  $\text{TiO}_2$  DNS, chemical bath deposition was conducted in a solution 40 mL of 0.25 M HCl and 1 mL of titanium(IV) *tert*-isopropoxide at 95 °C for 4 h.<sup>3,13</sup> The hematite films were deposited by CVD method in a 1 in. quartz tube inset into a two-temperature-zone furnace.<sup>14</sup> Iron(III) acetylacetonate, which was employed as the iron source, was loaded into the low-temperature zone of the furnace with the temperature of 125 °C. The vapor was then carried by a 500 sccm  $\text{N}_2/\text{O}_2$  flow into the higher-temperature zone of the furnace where the substrate was located. The substrate temperature and total pressure were maintained at 550 °C and 3 Torr, respectively.

The morphology of the nanostructures and films were examined by field-emission scanning electron microscopy (SEM, JEOL JSM-6700). Structural characterization of the hematite and hematite/ $\text{TiO}_2$  films were conducted using transmission electron microscopy (TEM, FEI E.O Tecnai F20 G2MAT S-TWIN Field Emission Gun Transmission Electron Microscope). The  $\text{TiO}_2$  CNS in hematite/ $\text{TiO}_2$  film was further evaluated from cross section employing high-angle annular dark-field scanning TEM (HAADF-STEM, JEOL-2100F CS STEM) and energy dispersive spectroscopy (EDS, EDAX PV 9840/10T). The structure, strain, and grain size of the hematite photoanodes were characterized by Raman scattering spectroscopy (integrated by Protrustech Corporation Limited) at an excitation length of 532 nm. Optical absorptions of the photoanodes were measured using a UV-vis-IR spectrophotometer (JASCO V-670). The surface potential images of the photoanodes were taken using scanning KPFM (Veeco diInnova) both in dark and under 532 nm light illumination. The details for KPFM measurements have been reported in our previous work.<sup>16</sup>

PEC performances of the hematite photoanodes were examined using a three-electrode system with a supporting electrolyte of 1 M KOH solution under simulated sunlight illumination at 100  $\text{mW cm}^{-2}$  from a 300 W xenon lamp (Newport 66983) coupled with an AM 1.5G filter (Newport 81094). The hematite photoanodes with a well-defined area of 1  $\text{cm}^2$ , Pt foil, and a nonaqueous Hg/HgO electrode were employed as the working, counter, and reference electrodes, respectively. The photos of the three-electrode PEC cell, hematite/ $\text{TiO}_2$  CNS/FTO photoanode, and Pt counter electrode during PEC water splitting are shown in Figure S1 (Supporting Information). PEC performances of the hematite photoanodes were also monitored using 0.5 M hydrogen peroxide as hole scavenger.

## RESULTS AND DISCUSSION

To form the hematite- $\text{TiO}_2$  heteronanostructures on the FTO substrates, the rutile  $\text{TiO}_2$  nanostructures, including DNS and CNS, are first grown on FTO substrates using wet chemical routes.<sup>3,13</sup> The top-view SEM images of the bare FTO,  $\text{TiO}_2$  DNS/FTO, and  $\text{TiO}_2$  CNS/FTO are shown in Figure 1a–c, respectively.  $\text{TiO}_2$  DNS, which is composed of separated nanorods (NRs) and tiny nanoparticles (NPs), is formed on the faceted surface of the FTO substrate using the hydrothermal method.  $\text{TiO}_2$  CNS, a continuous  $\text{TiO}_2$  NP layer, is constructed on the FTO substrate by combining hydrothermal and chemical bath deposition methods. Formation of rutile  $\text{TiO}_2$  CNS was confirmed by Raman characterization as shown in Figure S2 (Supporting Information). The feature of FTO

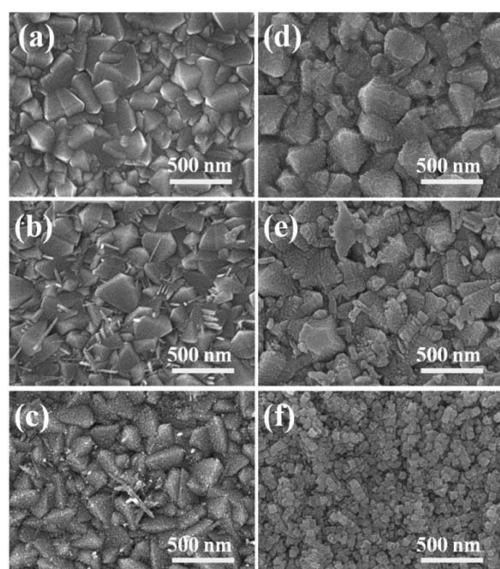


**Figure 1.** Top-view SEM images of (a) FTO, (b) TiO<sub>2</sub> DNS/FTO, (c) TiO<sub>2</sub> CNS/FTO, (d) hematite/FTO, (e) hematite/TiO<sub>2</sub> DNS/FTO, and (f) hematite/TiO<sub>2</sub> CNS/FTO.

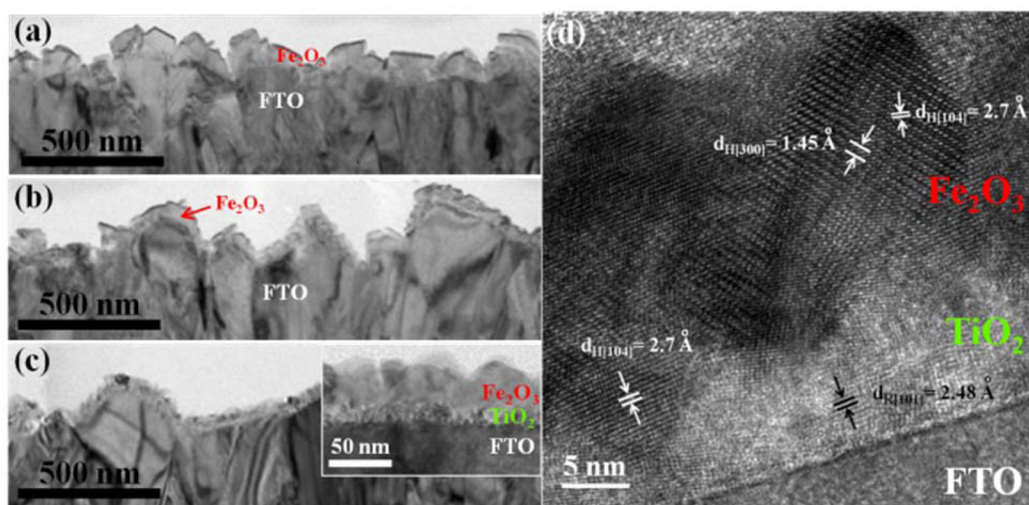
film remains apparent on the TiO<sub>2</sub>-modified FTO substrates, as shown in Figure 1b,c. Hematite films are further deposited on the three surfaces by CVD.<sup>14</sup> Figure 1d–f illustrates that the morphologies of the three hematite films are very different. The crystal size in the hematite layer deposited on the TiO<sub>2</sub> CNS/FTO substrate is smaller compared to those deposited on the other two substrates. For simplicity, the hematite films grown on the bare FTO, TiO<sub>2</sub> DNS/FTO, and TiO<sub>2</sub> CNS/FTO are, respectively, named as hematite/FTO, hematite/TiO<sub>2</sub> DNS/FTO, and hematite/TiO<sub>2</sub> CNS/FTO hereafter.

Figure 2a–c shows the cross-sectional TEM images of the hematite/FTO, hematite/TiO<sub>2</sub> DNS/FTO, and hematite/TiO<sub>2</sub> CNS/FTO, respectively. The thicknesses of these films on the FTO substrates are ~50–70 nm. TEM characterizations show that the hematite crystals with more faceted surface and relatively larger size are formed on the bare FTO and TiO<sub>2</sub> DNS/FTO substrates. Moreover, as shown in the inset of

Figure 2c, a layer of TiO<sub>2</sub> NPs with a thickness of ~10 nm exhibits between the hematite layer and FTO substrate. The high-resolution (HR) cross-sectional TEM image of the hematite/TiO<sub>2</sub> CNS/FTO is shown in Figure 2d. Lattice fringes are evidently illustrated in the HRTEM images. The *d* spacings estimated from the HRTEM image upon the FTO substrate can be sequentially referred to those of rutile TiO<sub>2</sub> and rhombohedrally centered hexagonal  $\alpha$ -Fe<sub>2</sub>O<sub>3</sub>. As shown in Figure S3 (Supporting Information), the HAADF-STEM image and TEM EDS mapping image also affirm the continuous TiO<sub>2</sub> NP layer between the FTO and hematite layer. In addition, the EDS mapping images show that there is no Ti signal appearing in the hematite layer. Therefore, both HRTEM and EDS characterizations indicate the formation of the high-quality hematite/TiO<sub>2</sub> heterostructure on the FTO substrate.

Structural characterizations of the three hematite films are also performed using Raman scattering spectroscopy. As shown in Figure S4 (Supporting Information), the appearances of two A<sub>1g</sub> (225 and 498 cm<sup>-1</sup>) and five E<sub>g</sub> (247, 293, 299, 412, and 613 cm<sup>-1</sup>) Raman scattering modes in the spectra confirm the formation of hexagonal  $\alpha$ -Fe<sub>2</sub>O<sub>3</sub> with the D<sub>3d</sub><sup>6</sup> crystal space group.<sup>18,19</sup> Moreover, the peak positions of these Raman scatterings of hematite/TiO<sub>2</sub> DNS/FTO and hematite/TiO<sub>2</sub> CNS/FTO show no obvious shift compared to those of hematite/FTO. This indicates the absence of additional strain in the hematite films deposited on the TiO<sub>2</sub> nanostructures compared to that on FTO substrate. However, the values of the full width at half-maximum (fwhm) of the E<sub>g</sub> peak at 299 cm<sup>-1</sup> in the spectra of hematite/FTO, hematite/TiO<sub>2</sub> DNS/FTO, and hematite/TiO<sub>2</sub> CNS/FTO photoanodes are 14.9, 15.1, and 16.4 cm<sup>-1</sup>, respectively. By showing the largest fwhm value, the grain size of the hematite film grown on the TiO<sub>2</sub> CNS/FTO substrate is confirmed to be the smallest one among the three films.<sup>20</sup>

To investigate the charge distribution in the hematite-TiO<sub>2</sub> heterostructure, in the present work, surface potential (SP) of the hematite/FTO and hematite/TiO<sub>2</sub>/FTO are measured in dark and under 532 nm light irradiation using KPFM.<sup>15,16</sup> Figure 3 shows the topographical images of the hematite/FTO and hematite/TiO<sub>2</sub>/FTO (a, c) as well as the corresponding SP images (b, d) measured in dark (lower panels) and with



**Figure 2.** Cross-sectional TEM images of (a) hematite/FTO, (b) hematite/TiO<sub>2</sub> DNS/FTO, and (c) hematite/TiO<sub>2</sub> CNS/FTO. (d) HRTEM image of hematite/TiO<sub>2</sub> CNS/FTO.

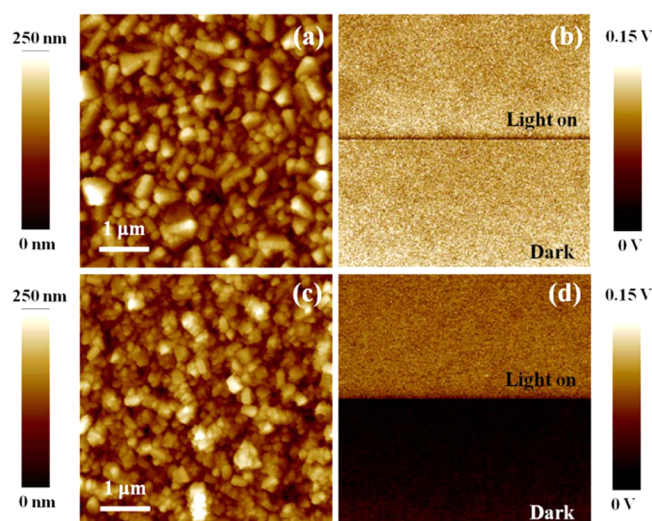


**Figure 3.** Topographical and the corresponding surface potential images of (a, b) hematite/FTO and (c, d) hematite/TiO<sub>2</sub>/FTO, respectively. SP images were taken in dark (lower) and with illumination (upper).

illumination (upper panels). As displayed in the lower panels of Figure 3b,d, in dark, the SP value of the hematite/TiO<sub>2</sub>/FTO is lower than that of hematite/FTO. Accordingly, compared to hematite/FTO, the Fermi level of the hematite is elevated in the hematite/TiO<sub>2</sub>/FTO.<sup>15,16</sup> As illustrated in Scheme 1a,b, this is attributed to the electron transfer from TiO<sub>2</sub> to hematite after junction formation until Fermi levels align at equilibrium. Therefore, the KPFM measurements confirm the formation of nN<sup>+</sup>  $\alpha$ -Fe<sub>2</sub>O<sub>3</sub>-TiO<sub>2</sub> heterojunction in the hematite/TiO<sub>2</sub>/FTO.

It has been demonstrated that the surface photovoltage (SPV) of photocatalyst, which is the modulation of the SP values measured under illumination and in dark, is associated with the excess carrier concentration on the surface of photocatalyst and is an index of the photocatalytic activity.<sup>16</sup> In this work, the SPVs of the hematite/FTO and hematite/TiO<sub>2</sub>/FTO can be further obtained from the differences of SP values of the upper panels (under illumination) and lower panels (in the dark) of Figure 3b,d to investigate the relative concentrations of steady-state excess carriers on the surfaces of the two hematite layers. As shown in Figure 3b, the SP values of the hematite/FTO measured under illumination and in dark are almost identical. This indicates that the concentrations of steady-state excess carriers on the surface of the illuminated hematite/FTO are very limited, resulting from significant photocarrier recombination in this hematite layer. On the other hand, as shown in Figure 3d, the increased SP value of the hematite/TiO<sub>2</sub>/FTO electrode is obtained under illumination compared to that measured in dark. The positive SPV value indicates significant amount of excess holes on the hematite surface of the heterojunction under illumination.<sup>16</sup> Compared to the hematite/FTO, the positive SPV measured in the hematite/TiO<sub>2</sub>/FTO reveals the enhancement of the charge separation in the hematite layer. It is attributed to the energy match in the nN<sup>+</sup>  $\alpha$ -Fe<sub>2</sub>O<sub>3</sub>-TiO<sub>2</sub> heterojunction for photoelectrons transferring from conduction band of hematite to that of TiO<sub>2</sub> and for photogenerated holes drifting to the surface of hematite. The KPFM investigation concludes the successful formation of the nN<sup>+</sup>  $\alpha$ -Fe<sub>2</sub>O<sub>3</sub>-TiO<sub>2</sub> heterojunction

with the energy-matched band structure facilitating charge separation, as illustrated in Scheme 1c.

The PEC performances of the hematite photoanodes on bare FTO and TiO<sub>2</sub>-modified FTO substrates are optimized in the aspect of the thickness of hematite layer, as shown in Figure S5 (Supporting Information). Notice that the characterizations shown in Figures 1–3 and Supporting Information, Figures S3 and S4 were conducted on the three optimized hematite photoanodes. Figure 4 shows the photocurrent density (*J*)–

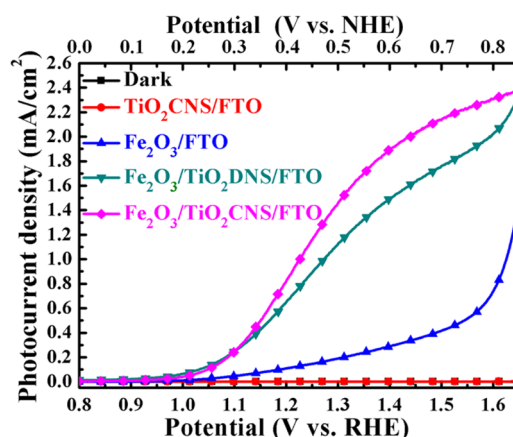


**Figure 4.** *J*–*V* curves of TiO<sub>2</sub> CNS/FTO, hematite/FTO, hematite/TiO<sub>2</sub> DNS/FTO, and hematite/TiO<sub>2</sub> CNS/FTO photoanodes with a scan rate of 5 mV s<sup>-1</sup> in a 1 M KOH electrolyte.

potential (*V*) curves of the three optimized hematite photoanodes obtained by linear sweep photovoltammetry measurements using a three electrode electrochemical configuration in 1 M KOH electrolyte. For comparison, the *J*–*V* curve of the TiO<sub>2</sub> CNS/FTO photoanode is also shown in Figure 4. At 1.23 V versus reversible hydrogen electrode (RHE), the photocurrent densities of the TiO<sub>2</sub> CNS/FTO, hematite/FTO, hematite/TiO<sub>2</sub> DNS/FTO, and hematite/TiO<sub>2</sub> CNS/FTO are 0.0005, 0.13, 0.79, and 1.1 mA cm<sup>-2</sup>, respectively. This shows that the contribution of solar-fuel conversion from the thin TiO<sub>2</sub> NP layer is almost negligible and that the PEC performances of the two hematite/TiO<sub>2</sub>/FTO photoanodes are superior to that of hematite/FTO photoanode. An eightfold enhancement of the photocurrent density is measured by introducing an interfacial TiO<sub>2</sub> CNS between the hematite layer and FTO substrate. Figure S6a,b (Supporting Information) show visual observation of the formation of bubbles on the hematite/TiO<sub>2</sub> CNS/FTO photoanode and Pt counter electrode, respectively, during PEC water splitting in the three-electrode system. Moreover, the production of oxygen through PEC water oxidation using the hematite/TiO<sub>2</sub> CNS/FTO photoanode is confirmed in a two-compartment, two-electrode PEC system by using a gas chromatograph (Supporting Information and Figure S7).

Figure 4 shows that the onset potentials of the three hematite photoanodes are nearly identical. It has been recognized that a large electrochemical overpotential required for hematite to drive water oxidation is ascribed to the slow hole kinetics of the oxygen evolution reaction at the interface of hematite and electrolyte as well as to the charge trapping in surface states.<sup>4,5</sup> Because of the same CVD growth condition for hematite layers, we suggest that the surface-state densities on the three hematite photoanodes are similar. Therefore, the onset potentials of the hematite-TiO<sub>2</sub> heterojunction photoanodes for water oxidation

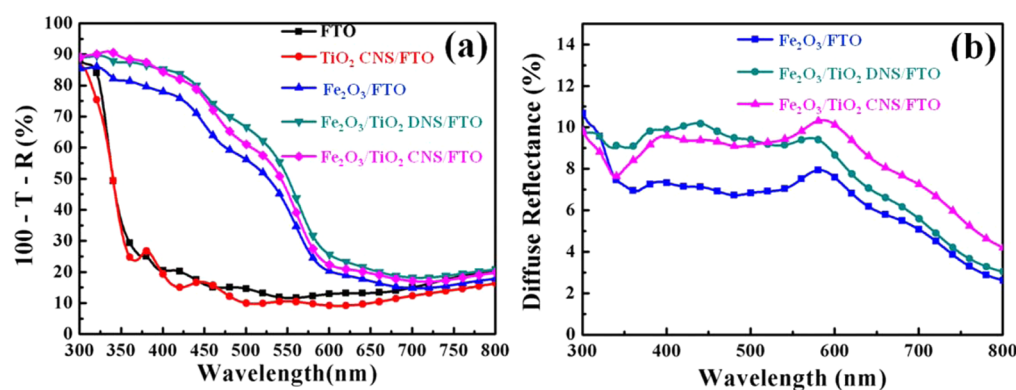


**Figure 5.** (a) Absorption spectra of FTO, TiO<sub>2</sub> CNS/FTO, hematite/FTO, hematite/TiO<sub>2</sub> DNS/FTO, and hematite/TiO<sub>2</sub> CNS/FTO. (b) Diffuse reflectance spectra of hematite/FTO, hematite/TiO<sub>2</sub> DNS/FTO, and hematite/TiO<sub>2</sub> CNS/FTO.

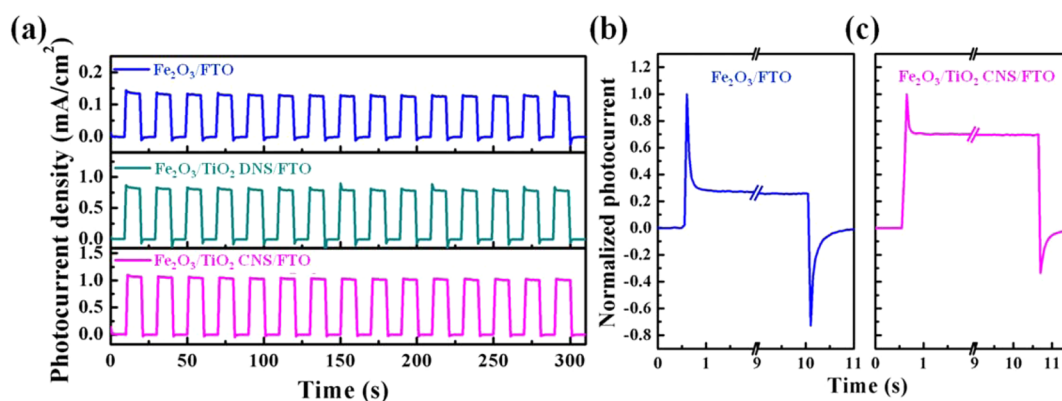


**Figure 6.** (a)  $J-t$  curves of hematite/FTO, hematite/TiO<sub>2</sub> DNS/FTO, and hematite/TiO<sub>2</sub> CNS/FTO photoelectrodes at an applied potential of 1.23 V vs RHE under illumination with 300 s light on/off cycles. Photocurrent transient behaviors of (b) hematite/FTO and (c) hematite/TiO<sub>2</sub> CNS/FTO in response to on-off irradiation.

are mainly determined by the slow hole kinetics of the oxygen evolution reaction regardless of the existence of built-in field in the heterojunction. The influence of built-in field in the hematite-TiO<sub>2</sub> heterojunction on the onset potential were investigated using hydrogen peroxide as a hole scavenger (Supporting Information), the details of which will be discussed later. Nevertheless, the  $J-V$  curves of the hematite/TiO<sub>2</sub>/FTO photoanodes demonstrate a steeper increase in current with respect to potential, which results from the faster charge separation occurring in the hematite-TiO<sub>2</sub> heterojunction due to the presence of the built-in potential.

The absorption spectra of hematite/FTO, hematite/TiO<sub>2</sub> DNS/FTO, and hematite/TiO<sub>2</sub> CNS/FTO obtained from the relation of  $(1 - \text{total transmittance } (T) - \text{total reflectance } (R))$  are shown in Figure 5a. For comparison, the absorption spectra of FTO substrate and TiO<sub>2</sub> CNS/FTO are also illustrated in this figure. Both bare FTO substrate and TiO<sub>2</sub> CNS/FTO show negligible light harvesting at wavelengths longer than 350 nm. Moreover, the three hematite photoanodes exhibit the absorption edge at  $\sim 590$  nm. When the hematite layers are deposited on the TiO<sub>2</sub>-modified substrates, the diffuse reflectance is slightly enhanced, as shown in Figure 5b. The photon absorption rates (expressed as current densities) of the hematite/FTO, hematite/TiO<sub>2</sub> DNS/FTO, and hematite/TiO<sub>2</sub> CNS/FTO under AM 1.5 at 100 mW cm<sup>-2</sup>, which are estimated from the absorption spectra in Figure 5a with the corresponding solar spectrum, are 8.4, 11.1, and 10.5 mA/cm<sup>2</sup>, respectively. This reveals that the light harvesting of the two

hematite films grown on TiO<sub>2</sub> nanostructure-modified FTO are similar, which are 25% enhanced compared to that on the bare FTO. With a thinner hematite film compared to hematite/FTO, the higher photon absorption rate in hematite/TiO<sub>2</sub> CNS/FTO may be attributed to the light scattering and reabsorption events taking place in the rough hematite films grown on the TiO<sub>2</sub> CNS modified substrates.

Figure 6a reveals the photoresponses of the hematite/FTO, hematite/TiO<sub>2</sub> DNS/FTO, and hematite/TiO<sub>2</sub> CNS/FTO over time, which were measured at an applied potential of 1.23 V versus RHE under chopped illumination. With the constant steady-state photocurrent density without decay in the light-on period of each cycle, the three photoelectrodes show the highly reproducible  $J-t$  patterns of light on/off cycles. The photocurrent transient behavior of the hematite/FTO and hematite/TiO<sub>2</sub> CNS/FTO photoanodes are shown in Figure 6b,c, respectively. After irradiation is suddenly switching on, as displayed in Figure 6b, significant photocurrent decay is observed in the normalized  $J-t$  curves of the hematite/FTO photoanode. The photocurrent decay is mainly attributed to holes trapped at surface states recombining with electrons from the conduction band.<sup>21</sup> Moreover, the obvious negative photocurrent density is also obtained in the  $J-t$  curves of the anode after the irradiation is suddenly switching off. It can be deduced from the negative photocurrent density that the holes accumulated at surface states keep recombining with electrons as the light switches off.<sup>22</sup> As shown in Figure 6c, the photocurrent decay and negative photocurrent density are

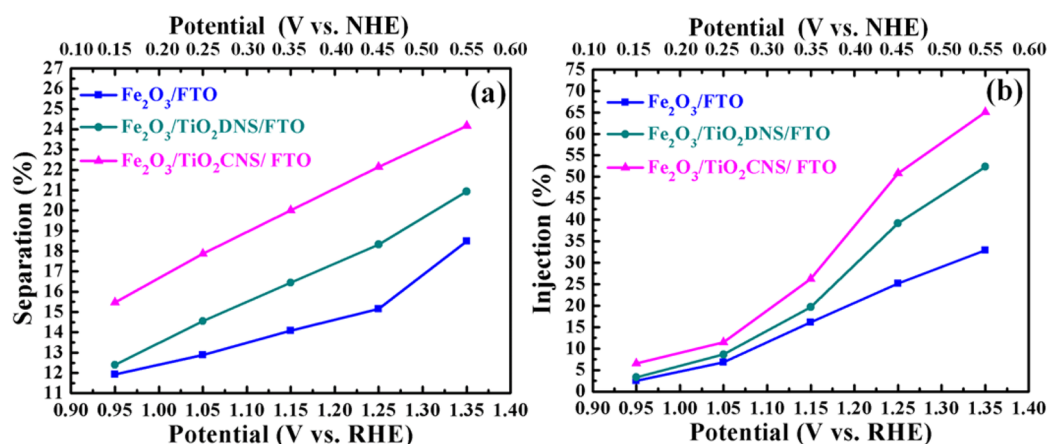


**Figure 7.** (a) Charge separation and (b) charge injection efficiencies of hematite/FTO, hematite/TiO<sub>2</sub> DNS/FTO, and hematite/TiO<sub>2</sub> CNS/FTO photoelectrodes.

substantially reduced in the  $J-t$  curve of the hematite/TiO<sub>2</sub> CNS/FTO photoanode, suggesting that the recombination of holes trapped at surface states with electrons from the conduction band can be efficiently suppressed in the hematite photoanode by the formation of hematite-TiO<sub>2</sub> CNS junction.

The charge separation and injection efficiencies of the hematite photoanodes were further investigated using hydrogen peroxide as a hole scavenger. It has been reported that by assuming the 100% injection efficiency of the photoanode with the addition of hydrogen peroxide in the electrolyte, the charge separation efficiency of the photoanode can be determined by the ratio of photocurrent density measured with H<sub>2</sub>O<sub>2</sub> in the electrolyte to the photon absorption rate.<sup>17,23,24</sup> Moreover, the charge injection efficiency of the photoanode can be estimated by the ratio of photocurrent densities measured without and with H<sub>2</sub>O<sub>2</sub> in the electrolyte. The details for the PEC measurements of the hematite/FTO, hematite/TiO<sub>2</sub> DNS/FTO, and hematite/TiO<sub>2</sub> CNS/FTO photoanodes with the addition of hydrogen peroxide in the electrolyte are shown in Figures S8 and S9 (Supporting Information).

With the addition of hydrogen peroxide in the electrolyte, as shown in Figure S8 (Supporting Information), the onset potential in the  $J-V$  curves of the hematite/TiO<sub>2</sub>/FTO photoanodes show a  $-50$  mV shift compared to that of hematite/FTO photoanode. Since the 100% hole injection efficiency of the photoanode is achieved, the influence of the surface traps on the PEC performance of the photoanode is absent by using hydrogen peroxide as a hole scavenger. Therefore, the onset potential shift toward the cathodic direction simply indicates the elevation of the quasi-Fermi level of the hematite/TiO<sub>2</sub>/FTO photoanodes. It is attributed to the established built-in potential in the nN<sup>+</sup>  $\alpha$ -Fe<sub>2</sub>O<sub>3</sub>-TiO<sub>2</sub> heterojunction, which has been confirmed by the results of KPFM measurements.

Figure 7a,b, respectively, show the charge-separation efficiencies and the charge-injection efficiencies of the three hematite photoanodes as functions of applied potential. Compared to the hematite/FTO, the charge separation efficiencies in the hematite/TiO<sub>2</sub>/FTO photoanodes are improved at the applied potentials ranging from 0.95 to 1.35 V versus RHE, as shown in Figure 7a. As the KPFM results demonstrated in Figure 3, the successful construction of the nN<sup>+</sup>  $\alpha$ -Fe<sub>2</sub>O<sub>3</sub>-TiO<sub>2</sub> heterojunction makes the charge separation efficiency increase in the hematite/TiO<sub>2</sub>/FTO photo-

anode. Moreover, compared to the hematite/TiO<sub>2</sub> DNS/FTO photoanode, the decrease of the hematite crystal size in the hematite/TiO<sub>2</sub> CNS/FTO photoanode reduces the recombination occurring within the crystals. It also contributes to the further increase of the fraction of the photogenerated holes reaching the interface of hematite and electrolyte.

The charge-injection efficiency is an index to examine the fraction of those holes at the interface of electrode and electrolyte injected into the electrolyte for water oxidation without recombining with electrons at surface traps.<sup>17</sup> The enhancement of charge-injection efficiency, as shown in Figure 7b, reflects that the reduction of charge recombination in the surface trap state is achieved in the nN<sup>+</sup>  $\alpha$ -Fe<sub>2</sub>O<sub>3</sub>-TiO<sub>2</sub> heterojunction photoanode. The surface trap state densities on the three hematite layers, which are deposited using the same CVD growth condition, are suggested to be similar. Therefore, the increase in charge-injection efficiency demonstrated in the hematite/TiO<sub>2</sub>/FTO photoanodes may be associated with the mechanisms regardless of the surface trap. We suggested that the formation of energy-matched nN<sup>+</sup>  $\alpha$ -Fe<sub>2</sub>O<sub>3</sub>-TiO<sub>2</sub> heterojunction mainly contributes to the enhancement of the charge-injection efficiency. With the built-in field in the heterojunction, the electric field in the hematite layer of the heterojunction photoanode is larger than that in the hematite/FTO photoanode at a given external potential. Consequently, far fewer photoelectrons remain in the hematite layer of the heterojunction photoanode due to considerably faster charge separation in the nN<sup>+</sup>  $\alpha$ -Fe<sub>2</sub>O<sub>3</sub>-TiO<sub>2</sub> heterojunction. The surface recombination rate is therefore reduced, and the lifetime of the surface trapped hole is prolonged as well. The loss of the photogenerated holes at the surface states through surface recombination with electrons can be significantly reduced because surface states have been fully occupied by the previously photogenerated holes, as shown in Scheme 1d. This mechanism of “charge-separation-enhanced injection” is also applicable to the fact that the charge-injection efficiency of each photoanode is increased with the applied potential, as shown in Figure 7b.

## CONCLUSION

An n-Fe<sub>2</sub>O<sub>3</sub> to n<sup>+</sup>-TiO<sub>2</sub> heterojunction is constructed on FTO substrate for use in PEC water oxidation. The TiO<sub>2</sub> nanostructure and high-quality hematite film are sequentially grown on FTO substrate via a wet chemical route and CVD

method, respectively. Surface potential measurements, which are conducted by KPFM in dark and under illumination, indicate the improvement of charge separation in hematite layer by the formation of energy-matched  $n\text{N}^+ \alpha\text{-Fe}_2\text{O}_3\text{-TiO}_2$  heterojunction. Significant improvement of PEC performance of the thin hematite photoanode is demonstrated in the hematite-TiO<sub>2</sub> heterojunction photoanode. Compared to the hematite photoanode, an eightfold enhancement of the photocurrent density at 1.23 V versus RHE is achieved in the hematite-TiO<sub>2</sub> heterojunction photoanode. The charge-separation and charge-injection efficiencies in the hematite-TiO<sub>2</sub> heterojunction photoanode, which are evaluated by using hydrogen peroxide as a hole scavenger in the electrolyte, are significantly higher than those in the hematite photoanode. We suggested that the formation of energy-matched  $n\text{N}^+ \alpha\text{-Fe}_2\text{O}_3\text{-TiO}_2$  heterojunction not only results in the improvement of charge-separation efficiency but also contributes to the enhancement of the charge-injection efficiency. Because of the considerably faster charge separation in the  $n\text{N}^+ \alpha\text{-Fe}_2\text{O}_3\text{-TiO}_2$  heterojunction, far fewer photoelectrons remain in the hematite layer of the heterojunction photoanode. The surface recombination rate is therefore reduced to prolong the lifetime of the surface-trapped holes, resulting in the increase in the injection efficiency.

## ■ ASSOCIATED CONTENT

### ■ Supporting Information

Photos of the three-electrode PEC cell, hematite/TiO<sub>2</sub> CNS/FTO photoanode, and Pt counter electrode during PEC water splitting, Raman spectrum of TiO<sub>2</sub> CNS/FTO, HAADF-STEM image and TEM EDS mapping images of hematite/TiO<sub>2</sub> CNS/FTO, Raman spectra of hematite/FTO, hematite/TiO<sub>2</sub> DNS/FTO, and hematite/TiO<sub>2</sub> CNS/FTO,  $J$ - $V$  curves of hematite/FTO and hematite/TiO<sub>2</sub> DNS/FTO photoanodes with various hematite thicknesses, detection of oxygen production through PEC water oxidation by the hematite/TiO<sub>2</sub> CNS/FTO photoanode using gas chromatography, PEC performances of hematite/FTO, hematite/TiO<sub>2</sub> DNS/FTO, and hematite/TiO<sub>2</sub> CNS/FTO photoanodes in 1 M KOH–0.5 M H<sub>2</sub>O<sub>2</sub> electrolytes. The Supporting Information is available free of charge on the ACS Publications website at DOI: 10.1021/acsaami.5b01489.

## ■ AUTHOR INFORMATION

### Corresponding Author

\*E-mail: wujj@mail.ncku.edu.tw.

### Author Contributions

The manuscript was written through contributions of all authors. All authors have given approval to the final version of the manuscript.

### Notes

The authors declare no competing financial interest.

## ■ ACKNOWLEDGMENTS

Financial supports from the Headquarters of Univ. Advancement at the National Cheng Kung Univ., which is sponsored by the Ministry of Education, Taiwan, and from Ministry of Science and Technology in Taiwan under Contract Nos. MOST 102-2221-E-006-215-MY3 and MOST 103-2221-E-006-245-MY3 are gratefully acknowledged.

## ■ REFERENCES

- (1) Grätzel, M. Photoelectrochemical Cells. *Nature* **2001**, *414*, 338–344.
- (2) Fujishima, A.; Honda, K. Electrochemical Photolysis of Water at a Semiconductor Electrode. *Nature* **1972**, *238*, 37–38.
- (3) Yang, J.-S.; Liao, W.-P.; Wu, J.-J. Morphology and Interfacial Energetics Controls for Hierarchical Anatase/Rutile TiO<sub>2</sub> Nanostructured Array for Efficient Photoelectrochemical Water Splitting. *ACS Appl. Mater. Interfaces* **2013**, *5*, 7425–7431.
- (4) Sivula, K.; Le Formal, F.; Grätzel, M. Solar Water Splitting: Progress Using Hematite ( $\alpha\text{-Fe}_2\text{O}_3$ ) Photoelectrodes. *ChemSusChem* **2011**, *4*, 432–449.
- (5) Lin, Y.; Yuan, G.; Sheehan, S.; Zhou, S.; Wang, D. Hematite-Based Solar Water Splitting: Challenges and Opportunities. *Energy Environ. Sci.* **2011**, *4*, 4862–4869.
- (6) Tilley, S. D.; Cornuz, M.; Sivula, K.; Grätzel, M. Light-Induced Water Splitting with Hematite: Improved Nanostructure and Iridium Oxide Catalysis. *Angew. Chem., Int. Ed.* **2010**, *49*, 6405–6408.
- (7) Lin, Y.; Zhou, S.; Sheehan, S. W.; Wang, D. Nanonet-Based Hematite Heteronanostructures for Efficient Solar Water Splitting. *J. Am. Chem. Soc.* **2011**, *133*, 2398–2401.
- (8) Lin, Y.; Xu, Y.; Mayer, M. T.; Simpson, Z. I.; McMahon, G.; Zhou, S.; Wang, D. Growth of p-Type Hematite by Atomic Layer Deposition and Its Utilization for Improved Solar Water Splitting. *J. Am. Chem. Soc.* **2012**, *134*, 5508–5511.
- (9) Le Formal, F.; Grätzel, M.; Sivula, K. Controlling Photoactivity in Ultrathin Hematite Films for Solar Water-Splitting. *Adv. Funct. Mater.* **2010**, *20*, 1099–1107.
- (10) Hisatomi, T.; Brillet, J.; Cornuz, M.; Le Formal, F.; Tetreault, N.; Sivula, K.; Grätzel, M. A Ga<sub>2</sub>O<sub>3</sub> Underlayer as an Isomorphic Template for Ultrathin Hematite Films Toward Efficient Photoelectrochemical Water Splitting. *Faraday Discuss.* **2012**, *155*, 223–232.
- (11) Hisatomi, T.; Dotan, H.; Stefik, M.; Sivula, K.; Rothschild, A.; Grätzel, M.; Mathews, N. Enhancement in the Performance of Ultrathin Hematite Photoanode for Water Splitting by an Oxide Underlayer. *Adv. Mater.* **2012**, *24*, 2699–2702.
- (12) Peng, L.; Xie, T.; Lu, Y.; Fan, H.; Wang, D. Synthesis, Photoelectric Properties and Photocatalytic Activity of the Fe<sub>2</sub>O<sub>3</sub>/TiO<sub>2</sub> Heterogeneous Photocatalysts. *Phys. Chem. Chem. Phys.* **2010**, *12*, 8033–8041.
- (13) Liao, W.-P.; Wu, J.-J. Wet Chemical Route to Hierarchical TiO<sub>2</sub> Nanodendrite/Nanoparticle Composite Anodes for Dye-Sensitized Solar Cells. *J. Mater. Chem.* **2011**, *21*, 9255–9262.
- (14) Wu, J.-J.; Lee, Y.-L.; Chiang, H.-H.; Wong, D. K.-P. Growth and Magnetic Properties of Oriented  $\alpha\text{-Fe}_2\text{O}_3$  Nanorods. *J. Phys. Chem. B* **2006**, *110*, 18108–18111.
- (15) Sung, Y.-H.; Frolov, V. D.; Pimenov, S. M.; Wu, J.-J. Investigation of Charge Transfer in Au Nanoparticle-ZnO Nanosheet Composite Photocatalysts. *Phys. Chem. Chem. Phys.* **2012**, *14*, 14492–14494.
- (16) Lin, W.-H.; Wu, J.-J.; Chou, M. M. C.; Chang, Y.-M.; Yoshimura, M. Charge Transfer in Au Nanoparticle–Nonpolar ZnO Photocatalysts Illustrated by Surface-Potential-Derived Three-Dimensional Band Diagram. *J. Phys. Chem. C* **2014**, *118*, 19814–19821.
- (17) Dotan, H.; Sivula, K.; Grätzel, M.; Rothschild, A.; Warren, S. C. Probing the Photoelectrochemical Properties of Hematite ( $\alpha\text{-Fe}_2\text{O}_3$ ) Electrodes Using Hydrogen Peroxide as a Hole Scavenger. *Energy Environ. Sci.* **2011**, *4*, 958–964.
- (18) de Faria, D. L. A.; Venâncio Silva, S.; de Oliveira, M. T. Raman Microspectroscopy of Some Iron Oxides and Oxyhydroxides. *J. Raman Spectrosc.* **1997**, *28*, 873–878.
- (19) Shim, S. H.; Duffy, T. S. Raman Spectroscopy of Fe<sub>2</sub>O<sub>3</sub> to 62 GPa. *Am. Mineral.* **2002**, *87*, 318–326.
- (20) Sundaram, O. N. B. *Thin Film Techniques and Applications*; Allied Publications: New Delhi, 2004.
- (21) Hagfeldt, A.; Lindström, H.; Södergren, S.; Lindquist, S.-E. Photoelectrochemical Studies of Colloidal TiO<sub>2</sub> Films: The Effect of Oxygen Studied by Photocurrent Transients. *J. Electroanal. Chem.* **1995**, *381*, 39–46.

(22) Le Formal, F.; Sivula, K.; Grätzel, M. The Transient Photocurrent and Photovoltage Behavior of a Hematite Photoanode under Working Conditions and the Influence of Surface Treatments. *J. Phys. Chem. C* **2012**, *116*, 26707–26720.

(23) Zhong, D. K.; Choi, S.; Gamelin, D. R. Near-Complete Suppression of Surface Recombination in Solar Photoelectrolysis by “Co-Pi” Catalyst-Modified W:BiVO<sub>4</sub>. *J. Am. Chem. Soc.* **2011**, *133*, 18370–18377.

(24) Rao, P. M.; Cai, L.; Liu, C.; Cho, I. S.; Lee, C. H.; Weisse, J. M.; Yang, P.; Zheng, X. Simultaneously Efficient Light Absorption and Charge Separation in WO<sub>3</sub>/BiVO<sub>4</sub> Core/Shell Nanowire Photoanode for Photoelectrochemical Water Oxidation. *Nano Lett.* **2014**, *14*, 1099–1105.